JOURNAL OF GEOPHYSICAL RESEARCH, VOL. 105, NO. D9, PAGES 11,767–11,780, MAY 16, 2000

Remote sensing of cloud properties using MODIS airborne simulator imagery during SUCCESS
1. Data and models

Bryan A. Baum,[1] David P. Kratz,[1] Ping Yang,[2] S.C. Ou,[3] Yongxiang Hu,[4,5]
Peter F. Soulen,[6,7] and Si-Chee Tsay[7]

Abstract. We investigate methods to infer cloud properties such as cloud optical thickness, thermodynamic phase, cloud particle size, and cloud overlap by comparing cloud and clear-sky radiative transfer computations to measurements provided by the Moderate Resolution Imaging Spectroradiometer (MODIS) airborne simulator (MAS). The MAS scanning spectroradiometer was flown on the NASA ER-2 during the Subsonic Aircraft Contrail and Cloud Effects Special Study (SUCCESS) field campaign during April and May 1996. The MAS bands chosen for this study correspond to wavelengths of 0.65, 1.63, 1.90, 2.15, 3.82, 8.52, 11, and 12 μm. Clear-sky absorption due to water vapor, ozone, and other trace gases is calculated using a set of correlated *k*-distribution routines developed specifically for these MAS bands. Scattering properties (phase function, single-scattering albedo, and extinction cross section) are derived for water droplet clouds using Mie theory. Scattering properties for ice-phase clouds are incorporated for seven cirrus models: cirrostratus, cirrus uncinus, cold cirrus, warm cirrus, and cirrus at temperatures of T = -20°C, -40°C, and -60°C. The cirrus are composed of four crystal types: hexagonal plates, two-dimensional bullet rosettes, hollow columns, and aggregates. Results from comparison of MAS data from a liquid water cloud with theoretical calculations indicate that estimates of optical thickness and particle size are reasonably consistent with one another no matter which spectral bands are used in the analysis. However, comparison of MAS data from a cirrus cloud with theoretical calculations shows consistency in optical thickness but not with particle size among the various band combinations used in the analysis. The methods described in this paper are used in two companion papers to explore techniques to infer cloud thermodynamic phase and cloud overlap.

1. Introduction

The retrieval of global cloud properties depends on accurate interpretation of satellite radiometric data. Retrievals of cirrus cloud properties from satellite-measured radiances are especially difficult because of the wide range of cirrus heights, particle sizes [*Heymsfield and Platt*, 1984; *Heymsfield et al.*, 1990], particle shapes [*Arnott et al.*, 1994; *Lawson et al.*, 1998] and their scattering properties [e.g., *Takano and Liou*, 1989a, b; *Yang et al.*, 1997; *Yang and Liou*, 1998], and the resulting large spatial and temporal variability of cirrus emittances and optical thicknesses [e.g., *Platt and Dilley*, 1979; *Sassen et al.*, 1990; *Spinhirne and Hart*, 1990; *Wielicki and Parker*, 1992]. The task of deriving cirrus properties from satellite data becomes even more difficult when cirrus appears simultaneously with other cloud types. Because of the difficulty in analyzing scenes that contain cloud overlap, operational cloud retrieval algorithms such as the International Satellite Cloud Climatology Project (ISCCP) by necessity employ the simplifying assumption that each satellite field of view (FOV) contains a single cloud layer.

The ability to remotely sense cloud properties will be enhanced when the new generation of cloud imagers are launched, beginning with an Earth-viewing sensor called the Moderate-Resolution Imaging Spectroradiometer (MODIS) that has been developed as the primary imager for the Earth Observing System-Terra and PM platforms. MODIS will provide images in 36 spectral bands between 0.415 and 14.2 μm with spatial resolutions of 250 m (two visible bands), 500 m (five bands), and 1000 m (29 bands). To support MODIS algorithm development, an aircraft version of the imager called the MODIS airborne simulator (MAS) has been installed and operated on the NASA high-altitude ER-2 research aircraft for a number of field campaigns, including SUCCESS, over a wide range of environmental conditions and surfaces.

The Subsonic Aircraft Contrail and Cloud Effects Special Study (SUCCESS) project conducted a multiaircraft field campaign during April and May 1996, primarily in close proximity to the Department of Energy (DOE) Atmospheric Radiation Measurement (ARM) program cloud and radiation test bed (CART) site. Among the goals of the project [*Toon and Miake-Lye*, 1998] are the investigation of the effect of aircraft

[1]NASA Langley Research Center, Hampton, Virginia.
[2]Science Systems and Applications, Inc., Lanham, Maryland.
[3]Department of Atmospheric Sciences, University of California at Los Angeles.
[4]Hampton University, Hampton, Virginia.
[5]Now at NASA Langley Research Center, Hampton, Virginia.
[6]Joint Center for Earth Systems Technology, University of Maryland Baltimore County, Catonsville.
[7]NASA Goddard Space Flight Center, Greenbelt, Maryland.

Paper number 1999JD901089.

exhaust and condensation trails (contrails) on the Earth's radiative energy balance, the formation of cirrus clouds, and heterogeneous atmospheric chemistry. This study focuses on the remote sensing of cloud properties, such as cloud thermodynamic phase, particle size, and optical thickness, in scenes containing both single-layered and multilayered clouds.

The goals of our investigation are to (1) build a theoretical framework for the inference of microphysical and optical properties for single-layered clouds in MAS imagery; (2) develop an improved cloud thermodynamic phase algorithm that exploits the difference in bulk absorption between ice and water by using visible and near-infrared bands (0.65, 1.63, and 1.90 μm) in addition to infrared bands (8.52, 11, and 12 μm); (3) investigate the retrieval errors when multilayered clouds are present instead of single-layer clouds; and (4) suggest a method to infer the presence of thin cirrus overlying lower-level clouds in the imagery (using the 1.90-, 1.63-, and 11-μm bands). Common to all of these goals is the requirement to establish a framework for comparing the radiative transfer calculations of clear- and cloudy sky conditions to the measurements made by the MAS during the SUCCESS field campaign on April 21, 1996. In this context the framework consists of radiative transfer models that account for atmospheric absorption/emission in each imager band, the proper development of cloud particle scattering properties, and finally, the inclusion of these properties in a discrete ordinates radiative transfer model.

Details of MAS-SUCCESS data are discussed in section 2. Microphysical models for ice-phase and water-phase clouds are presented in section 3, along with a discussion of the scattering properties for each cloud model. Atmospheric absorption and radiation models are discussed in section 4. A brief example comparing MAS data to radiative transfer simulations is presented in section 5. Section 6 summarizes and concludes part 1 of this study. A new algorithm for phase discrimination, based on two approaches proposed for use by MODIS, is presented in part 2 [*Baum et al.*, this issue] of this study, which also investigates the behavior of these techniques to discern phase when overlapping cloud layers are present in the imagery. In part 3 [*Baum and Spinhirne*, this issue] we present an approach for inferring pixels that contain thin cirrus overlap.

2. Data

The MAS is a scanning spectroradiometer with 50 spectral bands between 0.55 μm and 14.2 μm. The scan rate is 6.25 scans/s. Each scan line contains 716 Earth-viewing pixels with a maximum scan angle extending approximately 43° on either side of nadir. The spatial resolution is 50 m at nadir at a nominal ER-2 altitude of 20 km, as compared with the 250-1000 m (at nadir) resolution of the MODIS instrument on the EOS satellites. Beginning in 1995, the 8-bit data system was replaced with a 16-bit digitizer, enhancing the capability of the MAS instrument to simulate MODIS data. The entire set of MAS bands has been described by *King et al.* [1996].

To radiometrically calibrate the MODIS airborne simulator (MAS), a spectral calibration of each MAS band is performed. MAS spectral response function (SRF) shape and position are characterized in the laboratory using a monochromator-based measurement [*Moeller et al.*, 1997]. Spectral features in the measurements caused by absorption in the ambient laboratory atmosphere are corrected, as well as spectral position reporting error of the monochromator, to <0.5% of the MAS SRF at the half-power band width. The MAS emissive band linear calibration is accomplished through the use of two onboard blackbody sources viewed on each scan line during flight. The SRF measurements are used to convert the temperatures of the two onboard MAS blackbodies to equivalent Planck radiances. An emissivity correction to the MAS blackbodies is also applied [*Moeller et al.*, 1996]. In the reflectance bands, the SRF is used with integrating sphere measurements (in the laboratory) to compute a calibration slope and offset for application to inflight data [*King et al.*, 1996].

During SUCCESS the high-resolution interferometer sounder (HIS) [*Smith et al.*, 1996] also flew on the ER-2. The measurements from the MAS and HIS instruments were compared to assess MAS radiometric calibration accuracy. The MAS SRFs were convolved with the HIS radiance spectra and compared to MAS radiances averaged over the HIS spatial footprint. Radiometric biases were computed between MAS and HIS on five separate flights during SUCCESS. The MAS emissive band brightness temperatures were consistently within 1°C of the HIS measurements for atmospheric window bands.

3. Cloud Microphysical Models and Scattering Properties

Table 1 lists the MAS bands used in this study, the equivalent MODIS bands, MAS central wavelengths, and principal atmospheric absorbing species. The SRFs for four of these bands are provided in Figure 1. The SRFs are provided for comparison

Table 1. Spectral and Radiometric Characteristics of MAS Spectral Bands Used in This Study

MAS Band	Equivalent MODIS Bands	MAS Mean Wavelength (μm)	MAS Band FWHM (μm)	Principal Absorbing Components
2	1	0.65	0.05	H_2O, O_3
10	6	1.63	0.05	H_2O, CO_2, CH_4
15	-	1.90	0.05	H_2O
20	7	2.15	0.05	H_2O, CO_2, CH_4, N_2O
32	20	3.82	0.16	H_2O, CO_2, CH_4
42	29	8.52	0.40	H_2O, O_3, CH_4, N_2O
45	31	11.0	0.47	H_2O, CO_2
46	32	12.0	0.41	H_2O, CO_2

The term FWHM refers to full width, at half maximum bandwidth and is essentially the bandwidth between the 50% response points of the spectral response function for the band.

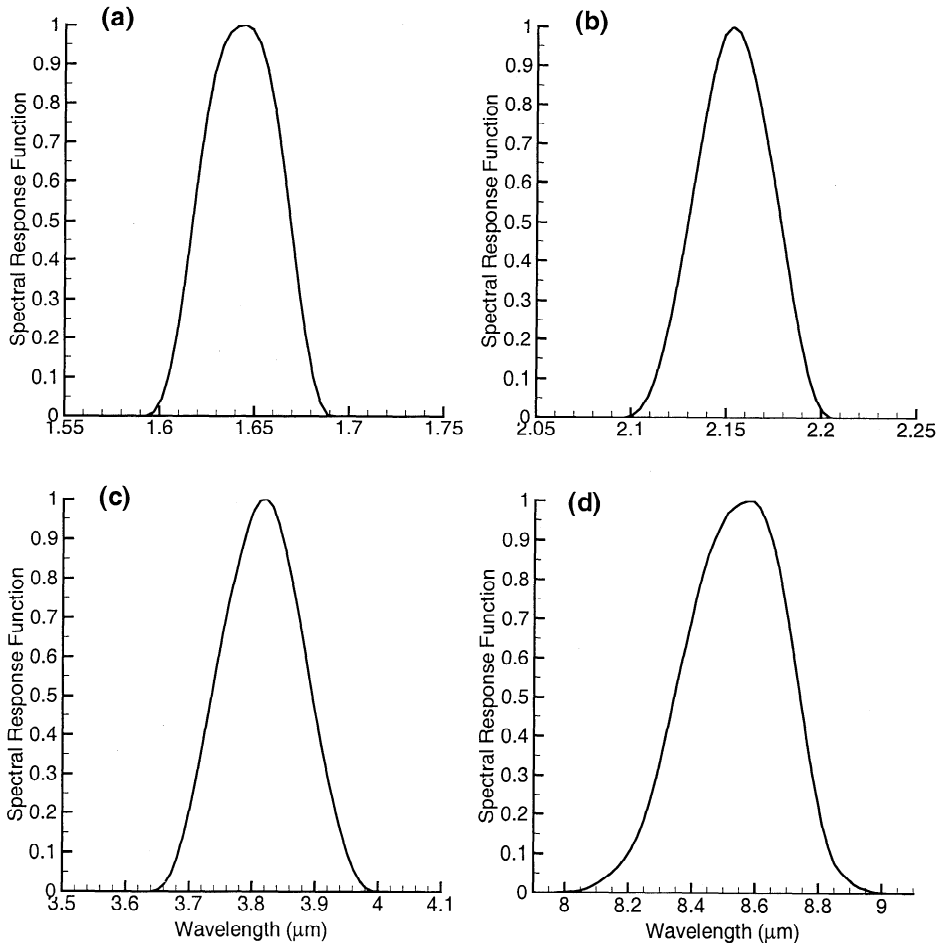

Figure 1. Spectral response functions for four MODIS airborne simulator (MAS) bands at (a) 1.63 μm, (b) 2.15 μm, (c) 3.82 μm, and (d) 8.52 μm.

with the imaginary indices of refraction for water and ice shown in Figure 2. *Gosse et al.* [1995] provide the most recent measured data of the ice refractive index, where the complex refractive index is defined as $m=m_r - im_i$. These data are supplemented by the published data by *Warren* [1984]. The water refractive index data are from *Downing and Williams* [1975]. For both water and ice the imaginary index of refraction m_i varies by almost an order of magnitude across the 1.63-μm band, but there is much less variation across the 8.52- and 11-μm bands.

For the MAS solar bands ($\lambda < 3$ μm), the central wavelength and mean refractive indices for water and ice are computed by weighting the spectral solar spectrum $S(\lambda)$ [*Kurucz et al.*, 1984; *Neckel and Labs*, 1984] with the MAS spectral response function $f(\lambda)$. For example, the mean imaginary index of refraction is computed from

$$\overline{m}_i = \frac{\int f(\lambda)S(\lambda)m_i(\lambda)d\lambda}{\int f(\lambda)S(\lambda)d\lambda}. \quad (1)$$

At IR wavelengths the band central wavelength and mean refractive indices are computed by replacing the solar spectrum $S(\lambda)$ with the Planck function $B(\lambda)$ that is representative of the thermal IR emission from the Earth. In the computation of the Planck function we used temperatures of 284 K and 233 K to represent water and ice clouds, respectively. Radiative transfer calculations are performed at the mean wavelength for each band using the mean indices of refraction to determine the scattering properties of both water- and ice-phase clouds.

3.1. Microphysical Models and Optical Properties

3.1.1. Water phase clouds. Water phase clouds are modeled as being composed of a modified gamma distribution of droplets having an effective radius r_{eff} ranging from 4 to 32 μm, and an effective variance of 0.1 [*Hansen and Travis*, 1974]. For each

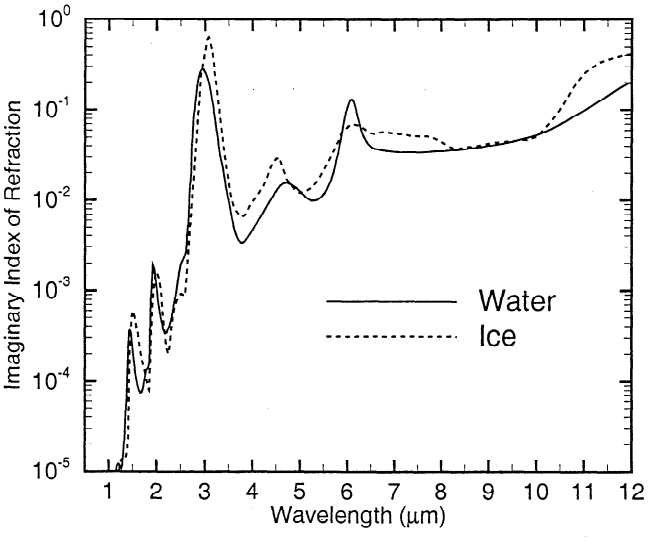

Figure 2. Imaginary indices of refraction for water (solid line) and ice (dashed line).

distribution, optical properties such as scattering phase function, single-scattering albedo (ω), and extinction cross section (C_{ext}) are calculated using Mie theory [*Wiscombe,* 1980]. For each distribution the scattering phase function is expressed by Legendre polynomials using a Fourier expansion in the azimuthal direction. The phase function may be expressed in the form

$$P(\cos\Theta) = \sum_{l=0}^{N} \tilde{\omega}_l P_l(\cos\Theta), \quad (2)$$

where Θ is the scattering angle and

$$P = (\mu, \phi; \mu', \phi') = \sum_{m=0}^{N} \sum_{l=m}^{N} \tilde{\omega}_l^m P_l^m(\mu)\, P_l^m(\mu') \cos m(\phi' - \phi). \quad (3)$$

The terms P_l^m are Legendre polynomials and

$$\tilde{\omega}_l^m = (2 - \delta_{0,m})\, \omega_l^m \frac{(l-m)!}{(l+m)!}, \quad (4)$$

for $l = m, \ldots, N$; $0 \le m \le N$; and $\delta_{0,m} = 1$ for $m=0$, $\delta_{0,m} = 0$ otherwise.

The microphysical and optical properties of the water phase clouds are provided in Table 2. Figure 3 shows the phase functions calculated at 0.65, 1.63, 3.82, and 8.52 μm for water clouds having r_{eff} = 4, 8, 16, and 32 μm. There are some commonalities between the phase functions at these wavelengths. The phase functions display a strong forward peak, a maximum at approximately 140° in scattering angle (the rainbow), and a maximum at a scattering angle of 180° (corresponding to the glory). There is little variation in the magnitude of the phase function at scattering angles between 10° and 60° and also in the rainbows. The magnitude of the phase function at 90°, corresponding to side scattering, is almost 2 orders of magnitude less than at the backscattering maximum. The effect of size distribution is most apparent in the scattering angle range between 60° and 120°. At 0.65 μm a second maxima appears at approximately 120° for larger r_{eff}. The features of the rainbow and glory are smoothed out when strong absorption is involved at 8.52 μm.

3.1.2. Ice phase clouds. Cirrus optical properties are derived for a set of seven ice crystal size distributions based on in situ measurements of cirrus. The cirrostratus (Cs) and cirrus uncinus distributions are described by *Heymsfield* [1975]. Two modified size distributions typical of warm and cold cirrus clouds are reported by *Heymsfield and Platt* [1984], as are three additional cirrus distributions that represent midlatitude cirrus at T = -20°C, T = -40°C, and T = -60°C. The seven size distributions cover a range of cloud microphysical properties and dynamical regimes, for example, production in slowly ascending parcels to 100 cm s^{-1} updrafts. Microphysical properties for the seven size distributions are shown in Table 3. To simplify the scattering calculations, the size distributions are discretized into five size bins similar to *Takano and Liou* [1989a].

The cirrus distribution effective size D_{eff} is defined as $D_{eff} = V/A$, where V is total volume and A is total projected area [*Wyser and Yang,* 1998]. This definition is related directly to ice water content (IWC) because V = IWC/ρ, where ρ is the density of ice. *Wyser and Yang* [1998] have shown that among various definitions of effective size, the aforementioned definition is most proper because the size distribution is not important in the determination of the bulk scattering properties of ice crystals.

For the present study, the cirrus distributions are composed of a combination of hexagonal plates, hollow columns, bullet rosettes, and aggregates (see Figure 4 for the shapes). *Yang et al.* [1997] provide a detailed explanation of the methods used to describe scattering calculations for hollow columns and bullet rosettes, and *Yang and Liou* [1998] describe calculations involving more complex crystals such as aggregates. For the scattering calculations a bullet rosette is assumed to be two-dimensional (planar) and composed of four branches, as shown in Figure 4. An aggregate crystal consists of hexagonal elements attached together in a random fashion. The number of elements in any particular aggregate lies between 2 and 8 and is chosen randomly. In the near future the current list of ice crystal shapes, or habits, will be increased to include spheres, solid columns, three-dimensional bullet rosettes, and aggregates composed of plates instead of columns.

Table 2. Microphysical Parameters and Optical Properties Used in Calculations For Mie Scattering Using a Modified Gamma Distribution of Water Droplets

r_{eff}	Wavelength (μm)	ω_o	C_{abs} $(\mu m)^2$	C_{ext} $(\mu m)^2$
4	0.65	1.0	0	79.3
	1.63	0.9976	0.2	85.2
	1.90	0.9722	2.4	87.9
	2.15	0.9912	0.8	92.5
	3.82	0.9692	3.57	115.9
	8.52	0.7459	12.5	49.0
	11.01	0.2914	19.2	27.1
	12.01	0.2218	29.3	37.6
8	0.65	1.0	0	306.5
	1.63	0.9950	1.6	322.0
	1.90	0.9446	18.1	325.8
	2.15	0.9806	6.4	328.8
	3.82	0.9211	27.3	346.0
	8.52	0.7768	88.7	397.4
	11.01	0.4400	118.3	211.4
	12.01	0.3524	152.0	234.7
10	0.65	1.0	0	475.3
	1.63	0.9939	3.0	495.5
	1.90	0.9330	33.6	500.7
	2.15	0.9760	12.1	504.7
	3.82	0.9040	50.8	528.7
	8.52	0.7550	160.7	656.0
	11.01	0.4747	204.1	388.6
	12.01	0.3871	247.7	404.2
16	0.65	1.0	0	1200.7
	1.63	0.9906	11.6	1237.6
	1.90	0.9013	123.0	1246.5
	2.15	0.9635	45.7	1253.7
	3.82	0.8623	178.9	1298.8
	8.52	0.6501	522.9	1494.6
	11.01	0.5151	602.6	1243.0
	12.01	0.4410	658.2	1177.4
32	0.65	1.0	0	4739.2
	1.63	0.9824	85.2	4830.5
	1.90	0.8301	824.5	4852.1
	2.15	0.9330	326.1	4868.9
	3.82	0.7769	1110.6	4978.0
	8.52	0.5348	2435.8	5236.3
	11.01	0.5052	2581.2	5216.2
	12.01	0.4815	2569.1	4954.8

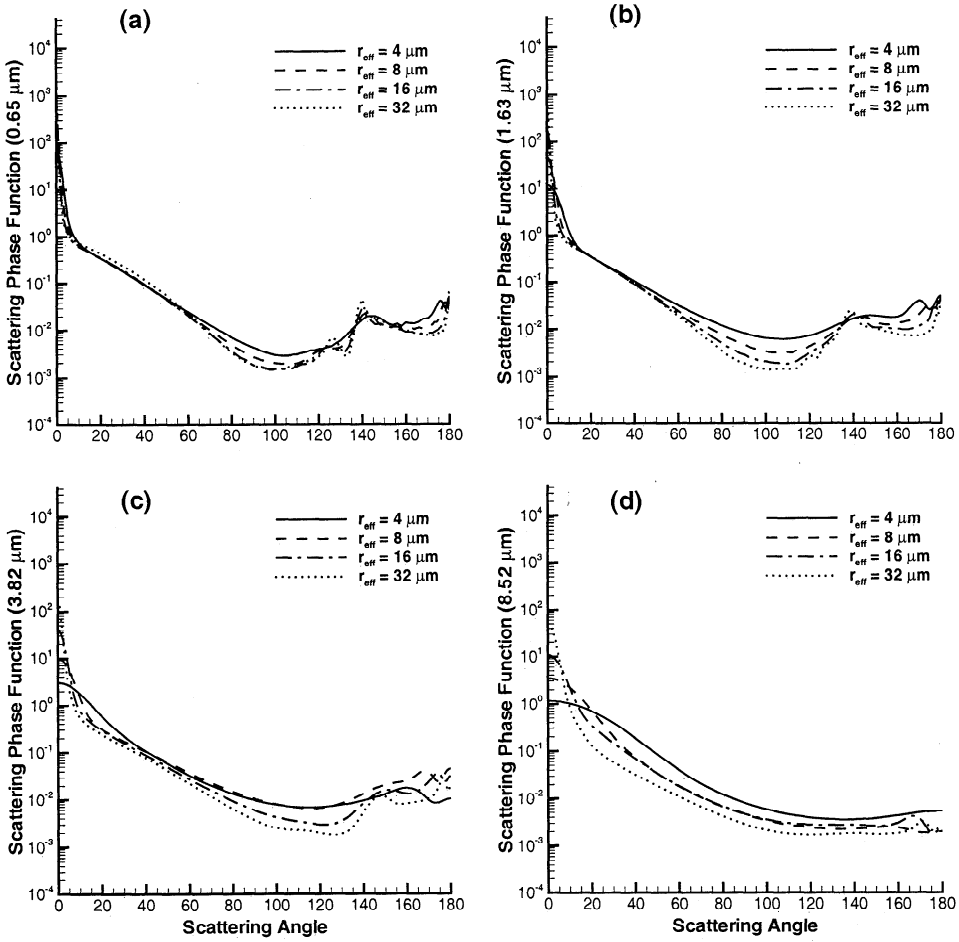

Figure 3. Scattering phase functions at various wavelengths for a water-phase cloud composed of a modified gamma distribution of droplet sizes with an effective radius r_{eff} = 4, 8, 16, and 32 μm, with each having an effective variance of 0.1.

Detailed information is unavailable concerning ice crystal habit and percentage of each individual habit for a given size distribution. On the basis of the percentages of each habit from replicator data collected during the first ISCCP regional experiment (FIRE II) intensive field observation (IFO) we have chosen the following method to model various cirrus clouds for the purposes of deriving scattering properties. When the maximum dimension D is small (D < 70 μm), i.e., for small ice crystals, the percentage of ice crystals within the size region is assumed to be composed of 50% bullet rosettes, 25% hexagonal plates, and 25% hollow columns. When D > 70 μm, the percentage of ice crystals within the size region is assumed to be composed of 30% aggregates, 30% bullet rosettes, 20% hexagonal plates, and 20% hollow columns. The single-scattering calculations are performed using a combination of the improved geometric optics method (GOM2) and the finite difference time domain (FDTD) techniques discussed by *Yang and Liou* [1996a, b]. The FDTD is applied to particles having a size parameter smaller than 10, whereas GOM2 is employed for size parameters larger than 10. Scattering properties for the seven cirrus distributions are shown in Table 4.

Scattering phase functions for the seven cirrus ice crystal distributions are shown in Figures 5a–5d for λ = 0.65 μm, 1.63 μm, 3.82 μm, and 8.5 μm, respectively. The phase functions at 11 μm and 12 μm are similar in shape to those at 8.52 μm and are not shown here. At each wavelength the phase functions for the seven cirrus distributions have similar shapes but different magnitudes. At 0.65 μm the ice-crystal phase functions have a strong forward scattering peak due to both diffraction and by δ-function transmission through parallel planes at Θ = 0° [*Takano and Liou*, 1989a]. The phase functions displayed in Figure 5 do not include the contribution due to δ-function transmission. With a cirrus ice crystal distribution composed solely of smooth hexagonal ice crystals, the scattering phase function at 0.65 μm displays maxima corresponding to inner and

Table 3. Microphysical Characteristics of Seven Ice-Crystal Size Distributions

Model Description	Mean Effective Size (μm)	Ice Water Content (g/m^3)
Cirrostratus (Cs)	19.3	0.183*E*-02
Ci uncinus	78.5	0.712*E*-01
Ci (cold)	8.9	0.352*E*-03
Ci (warm)	26.3	0.454*E*-02
Ci (*T*=-20°C)	33.3	0.441*E*-02
Ci (*T*=-40°C)	37.3	0.491*E*-02
Ci (*T*=-60°C)	12.7	0.231*E*-03

Read 0.183*E*-02 as 0.183×10^{-2}.

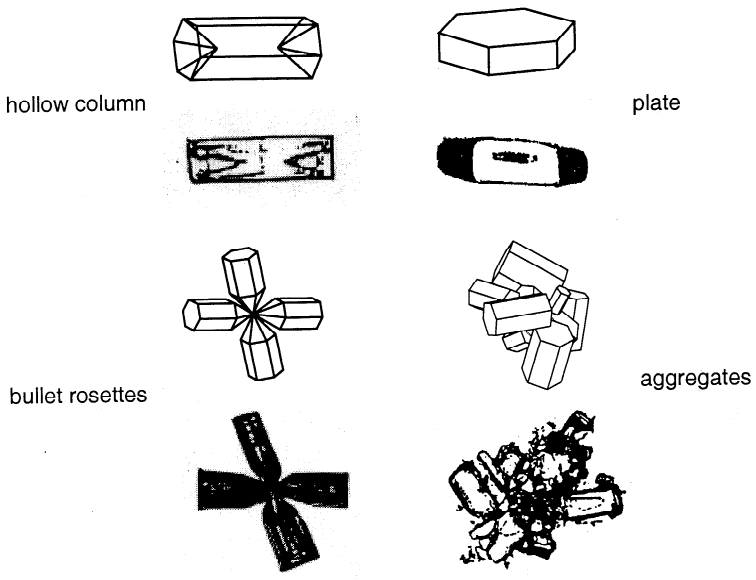

Figure 4. Ice-crystal shapes employed in the calculation of scattering properties for the seven cirrus cloud models.

outer halos at 22° and 46°, respectively [e.g., *Takano and Liou*, 1989a]. When rough particles are included in the ice crystal distribution, such as bullet rosettes and aggregates, the maxima at 22° and 46° are reduced from those shown by *Takano and Liou* [1989a], which did not include rough particles. In fact, the outer halo at 46° is almost nonexistent for the cold cirrus distribution. There is a slight relative peak near 156° that is similar to but displaced from the rainbow feature noted in the water droplet phase function (Figure 3a) which occurs at 140°. The magnitude of side scattering is comparable to that of backscattering, in contrast with the phase functions shown for water droplet distributions.

The scattering phase functions at 1.63 μm show a strong forward scattering peak and also a relative increase in magnitude

Table 4. Microphysical Properties for Seven Cirrus Models

λ (μm)	m_r	m_i	Optical properties	Cs	Ci					
					Uncinus	(Cold)	(Warm)	(*T*=-20°C)	(*T*=-40°C)	(*T*=-60°C)
0.65	1.308	0.1365*E*-07	β_e	0.206	1.962	0.0824	0.3707	0.2869	0.2858	0.3864
			ω	0.999995	0.9999	0.999997	0.999994	0.999993	0.999992	0.999997
			g	0.8009	0.8443	0.7487	0.7902	0.8045	0.8135	0.7674
1.63	1.288	0.2529*E*-03	β_e	0.204	1.951	0.2833	0.3769	0.2846	0.2833	0.3840
			ω	0.9720	0.9055	0.9508	0.9643	0.9561	0.9508	0.9811
			g	0.7911	0.8791	0.8239	0.7969	0.8119	0.8239	0.7676
1.90	1.278	0.4108*E*-03	β_e	0.2095	1.971	0.0846	0.3769	0.2906	0.2889	0.3951
			ω	0.9592	0.8713	0.9800	09497	0.9385	0.9310	0.9724
			g	0.8020	0.8933	0.7635	0.8071	0.8226	0.8353	0.7772
2.15	1.268	0.6858*E*-03	β_e	0.2136	1.9866	0.0866	0.3840	0.2954	0.2933	0.0404
			ω	0.9491	0.8443	0.9749	0.9382	0.9246	0.9154	0.9656
			g	0.8107	0.9045	0.7706	0.8151	0.8310	0.8443	0.7848
3.82	1.387	0.7439*E*-02	β_e	0.214	1.965	0.2137	0.3937	0.2980	0.2926	0.4235
			ω	0.7924	0.6347	0.7924	0.7927	0.7613	0.7376	0.8488
			g	0.7840	0.9242	0.7840	0.7777	0.8039	0.8257	0.7358
8.52	1.291	0.03909	β_e	0.2101	0.1978	0.0778	0.3631	0.2860	0.2855	0.3753
			ω	0.6966	0.5737	0.7574	0.6867	0.6659	0.6473	0.7344
			g	0.8424	0.9482	0.7551	0.8278	0.8558	0.8750	0.7865
11.01	1.103	0.2493	β_e	0.1689	1.946	0.0554	0.2980	0.2436	0.2517	0.2803
			ω	0.4822	0.5373	0.4124	0.4761	0.4934	0.5044	0.4409
			g	0.9204	0.9650	0.8557	0.9174	0.9313	0.9400	0.8846
12.01	1.285	0.414	β_e	0.1963	2.203	0.0717	0.3481	0.2764	0.2799	0.3475
			ω	0.5412	0.5678	0.5021	0.5339	0.5440	0.5501	0.5170
			g	0.8905	0.9349	0.8369	0.8849	0.8987	0.9075	0.8583

The units of the extinction coefficient β_e are km^{-1}.

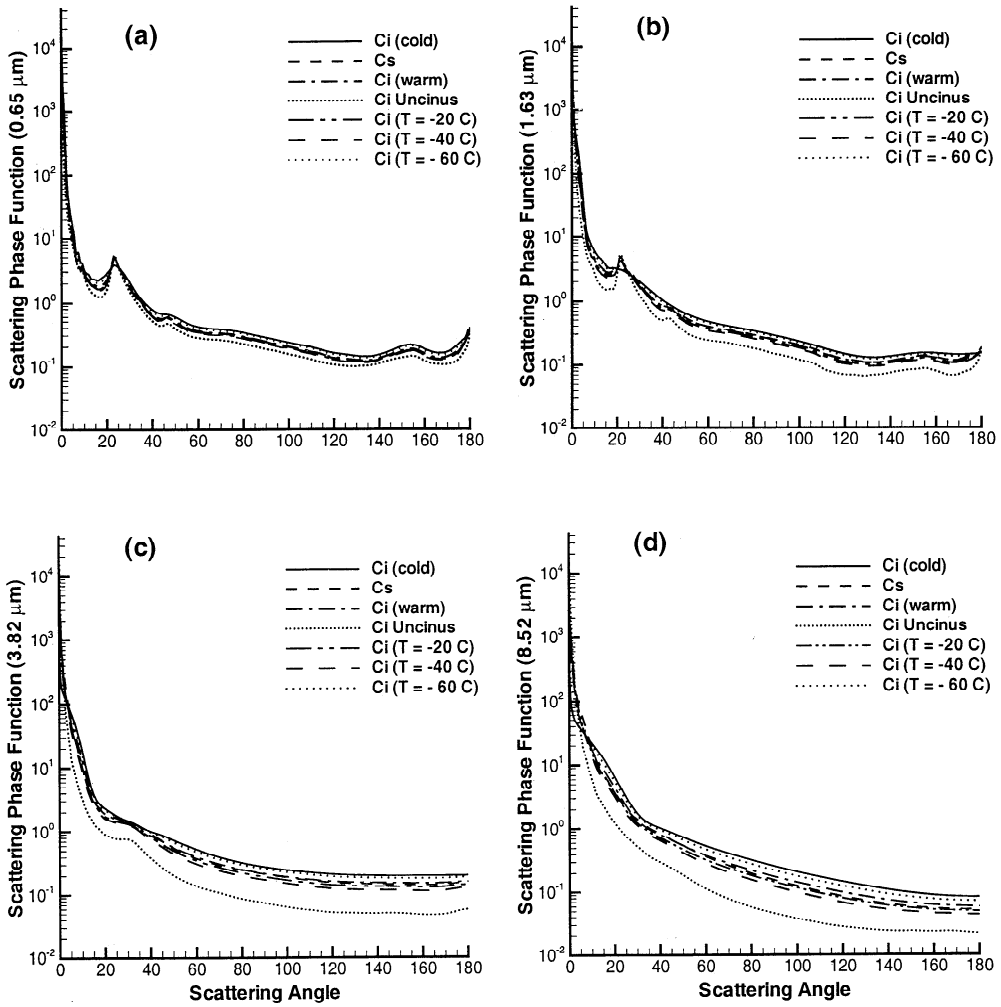

Figure 5. Scattering phase functions for seven various cirrus cloud particle size and habit distributions. (a) $\lambda = 0.65$ μm, (b) $\lambda = 1.63$ μm, (c) $\lambda = 3.82$ μm, (d) $\lambda = 8.52$ μm. Effects of δ transmission are not included.

for the inner halo at 22°. However, the magnitudes of the peaks at 46° and 156° are reduced further from those noted at 0.65 μm.

At 3.82 μm the peak at 22° is difficult to detect for the cold cirrus distribution but is still present for the distributions associated with the warmer clouds. There is no apparent outer halo at 46° for any of the cirrus distributions, nor is there any discernable maximum in the backscatter region at 156°.

For the IR wavelengths (8.5 μm, 11 μm, and 12 μm) the phase functions demonstrate a strong forward peak that decreases monotonically with increasing scattering angle. At the NIR and IR wavelengths the magnitude of the side scattering is comparable to that of backscattering.

4. Radiation and Atmospheric Absorption Models

4.1. Treatment of Atmospheric Molecular Absorption

The radiances measured by the MAS instrument are noticeably affected by molecular absorption occurring within the atmosphere. To ensure the proper interpretation of the measurements, correlated *k*-distribution routines have been created to account for the observed molecular absorption. Since the correlated *k*-distribution routines have been tailored specifically to the MAS bands, these routines are assured of being representative of the molecular absorption observed by these instruments. In addition to being fast and accurate, the correlated *k*-distribution routines have been constructed to accommodate the very long pathlengths encountered in multiple-scattering routines. The important absorbers for the selected MODIS/MAS bands are presented in Table 1.

The exponential-sum fitting of transmissions (ESFT) procedure [*Kratz*, 1995] is used to derive the *k*-distribution coefficients for the MAS bands in Table 1. *Kratz* [1995] presents a thorough step-by-step description of the ESFT procedure that is based upon the least squares procedure of *Press et al.* [1986]. This ESFT procedure has proved to be very effective in the derivation of the *k*- distribution coefficients used in satellite retrieval routines.

Kratz and Rose [1999] demonstrated that the *k*-distribution coefficients produced by the present ESFT procedure are representative of realistic distributions of the absorption coefficient versus calculated cumulative probability of the absorption coefficients. Once constructed, the MAS correlated *k*-distribution routines were tested against reference line-by-line calculations for a variety of clear-sky cases. The accuracies of the correlated *k*-distribution calculations tended to be within 1% for the case of the upwelling clear-sky radiances.

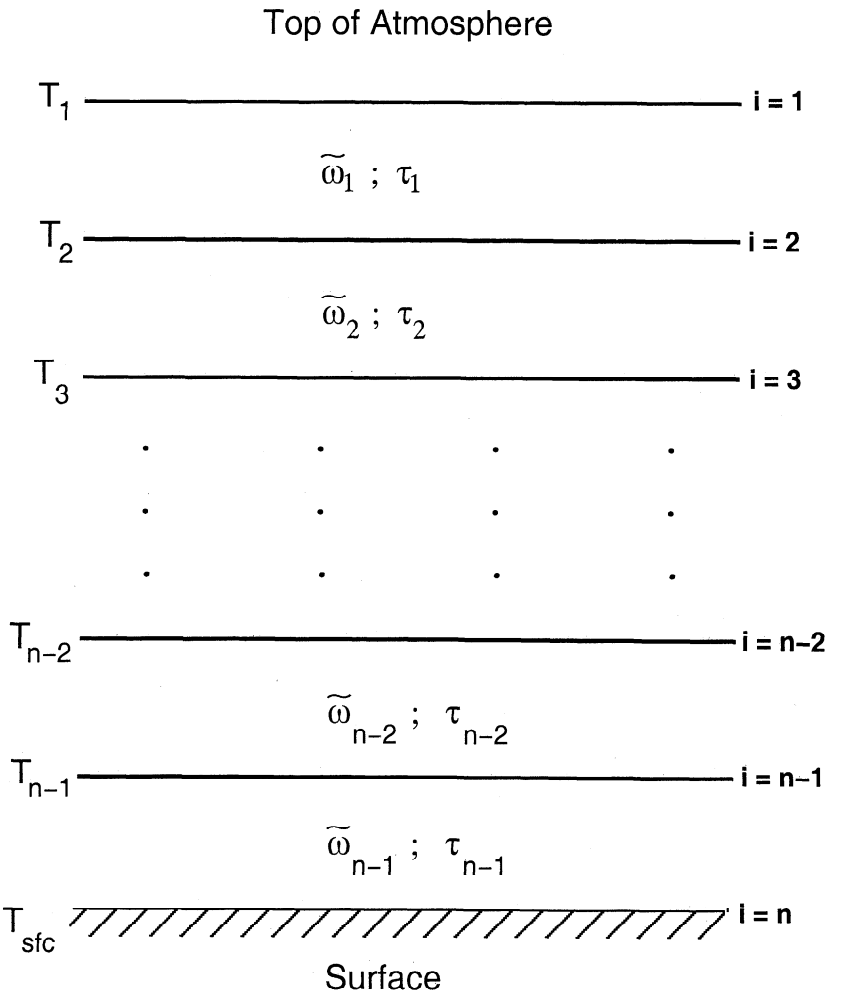

Figure 6. Schematic of a model atmosphere used in the discrete ordinates radiative transfer (DISORT) model.

4.2. Discrete Ordinates (DISORT) Model

The discrete ordinates radiative transfer (DISORT) model [*Tsay et al.*, 1990] is used to calculate the top-of-atmosphere (TOA) radiances expected for a range of clear and cloudy conditions for the wavelengths listed in Table 1. The atmosphere is composed of a discrete number of adjacent homogeneous layers as shown in Figure 6. The single-scattering albedo and optical thickness are constant within each layer but may vary from layer to layer. For the 1.63-, 1.90-, 2.15-, 3.82-, 8.5-, 11-, and 12-μm bands the atmosphere is divided into 20 layers, with 0.5-km resolution between the surface and the 5-km and 1-km resolution from 5 km to 15 km. For each layer the correlated *k*-distribution routines discussed in section 4.1 are implemented to calculate optical thicknesses due to gaseous absorption. A set of input temperature, humidity, and ozone profiles from rawinsonde measurements for a typical day during SUCCESS is used to compute atmospheric absorption associated with each *k*.

For the 0.65-μm band, where ozone is the principal absorber and Rayleigh scattering is important, the atmosphere is modeled with either four or six layers, depending on whether there is one cloud layer or two, respectively. The first (uppermost) layer includes the effect of ozone absorption and Rayleigh scattering from the tropopause to the top of the atmosphere. The second layer includes Rayleigh scattering between the top of the uppermost cloud and the tropopause. The third layer contains the optical properties for either a water- or an ice-phase cloud. The layer below the cloud contains Rayleigh scatterers. For cases when a second cloud layer is desired, a buffer layer of Rayleigh scatterers is included between the upper and the lower cloud layers. Aerosol contributions are neglected in this study.

When a phase function displays a strong forward peak, it may be necessary to truncate and renormalize the phase function before expansion into a Legendre polynomial series to reduce the number of terms necessary in the radiative transfer calculations. If the phase function is truncated, the scattering properties are adjusted using a procedure described in the Appendix.

The temperature and humidity profile presented in Figure 7 is taken from a rawinsonde launched from the ARM CART site at 1700 UTC on April 21, 1996, and is used for all simulations shown in section 5, as a basis for both the water- and the ice-cloud simulations. Comparisons of the model with more extensive data sets will appear in future papers.

5. Results

5.1. Water-Phase Clouds

Our intent is to provide a theoretical framework for performing radiative transfer calculations over land and cloud surfaces. The approach is illustrated with a specific case of a

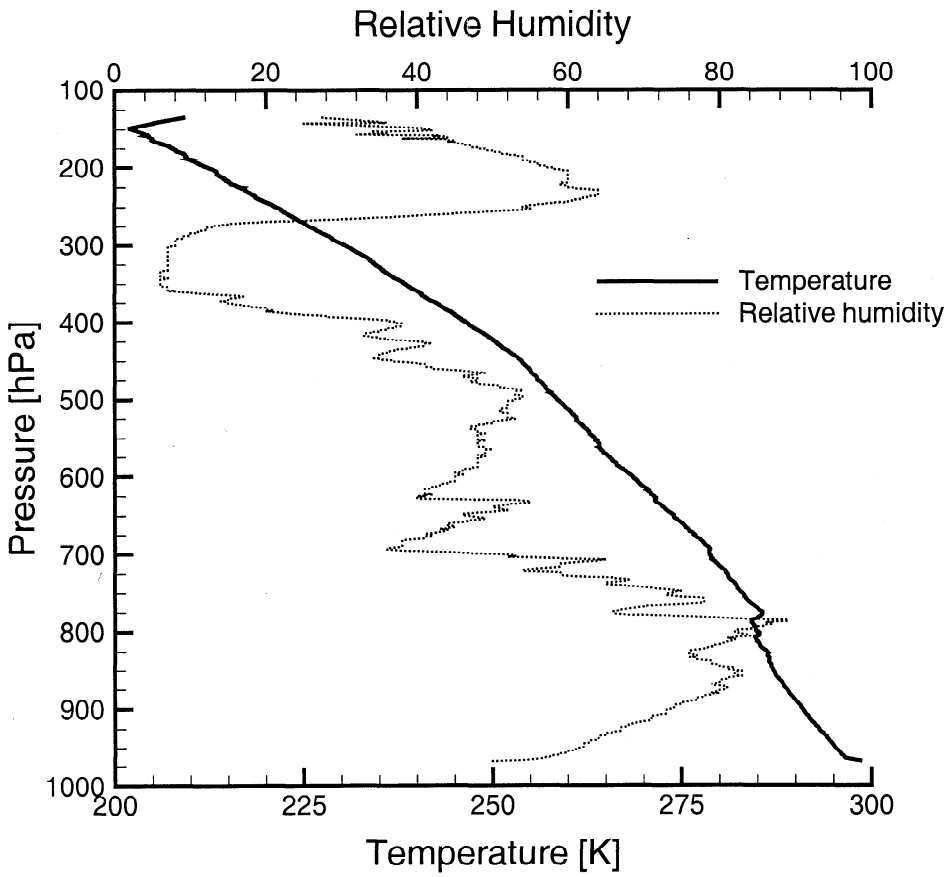

Figure 7. Sonde profile measured at the atmospheric radiation measurement cloud and radiation testbed (ARM CART) site on April 21, 1996, and 2000 UTC. Temperature is denoted by the solid line, while relative humidity is denoted by the dotted line.

flight track recorded on April 21, 1996, over northern Oklahoma within 50 km of the ARM CART site. A segment of this flight track is shown in Figure 8 at three wavelengths: 0.65 μm, 1.63 μm, and 1.90 μm. The scale of the image is 37.5 km cross track by 50 km along track. In the 0.65-μm image the surface is dark, and low clouds are very bright with relatively sharp edges. Cirrus clouds are wispy, have less distinct boundaries, and typically display few textural details. At 1.63 μm the vegetated surface is much brighter than at 0.65 μm since there is no chlorophyll absorption. The surface generally consists of cropland, with a meandering river in the center of the image. Cloud shadows are very apparent in the 1.63-μm image. The 1.63-μm reflectance for a shadowed clear-sky pixel may decrease by more than half of that of a nonshadowed clear-sky pixel. The presence of very distinct shadows in the 1.63-μm image can be used as a rough indicator of cloud height; low clouds cast much shorter and, typically, more distinct shadows than the cirrus. The 1.90-μm band is located near a band of strong water vapor absorption and is sensitive to upper tropospheric water vapor. Since cirrus are located typically above most of the atmospheric water vapor, the MAS imager is able to receive an increased amount of scattered solar energy if high-level clouds are present. The 1.90-μm image is provided to show evidence for thin cirrus in the image. Further discussion of the 1.90-μm band is provided by *Baum et al.*, part 2 [this issue].

Two regions from Figure 8 are selected for detailed analysis: one from a low-level water cloud (region A) and the second from cirrus (region B). Radiative transfer calculations are performed for a water-phase cloud having a cloud-top temperature of 284 K. Surface albedos at 0.65, 1.63, and 3.82 μm are chosen to be 0.11, 0.22, and 0.1, respectively, based on averaged MAS reflectance measurements over regions of clear sky. The surface is assumed to be a Lambertian reflector with a temperature of 302 K. Surface emissivity is taken to be 0.985 at the IR wavelengths since the surface contains varying amounts of vegetation at this time of year. The solar zenith angle is 32°, and the viewing zenith angle is 0°.

A comparison of MAS data with theory is presented in Figure 9 for four different band combinations. In each of the four panels of Figure 9, cloud optical thicknesses at each wavelength are related to that at the visible band by the ratio of the extinction cross sections. To simplify interpretation of the results, 0.65-μm (visible) optical thicknesses are denoted for one of the curves in each panel of the figure. The MAS measurements from region A are denoted as squares. Figures 9a and 9b compare theoretical calculations with the MAS measurements of 1.63- and 2.15-μm reflectances, respectively, as a function of 0.65-μm reflectance and 0.65-μm cloud optical thickness. MAS data displaying high reflectances may be interpreted as belonging to the opaque clouds having an effective radius of less than 4 μm. The MAS data tend to follow a linear pattern between clear-sky and opaque cloud conditions. One explanation may be that the MAS data are collected from a cumulus cloud that (1) is clearly not plane parallel, having cloud edges, and (b) clearly contains three-

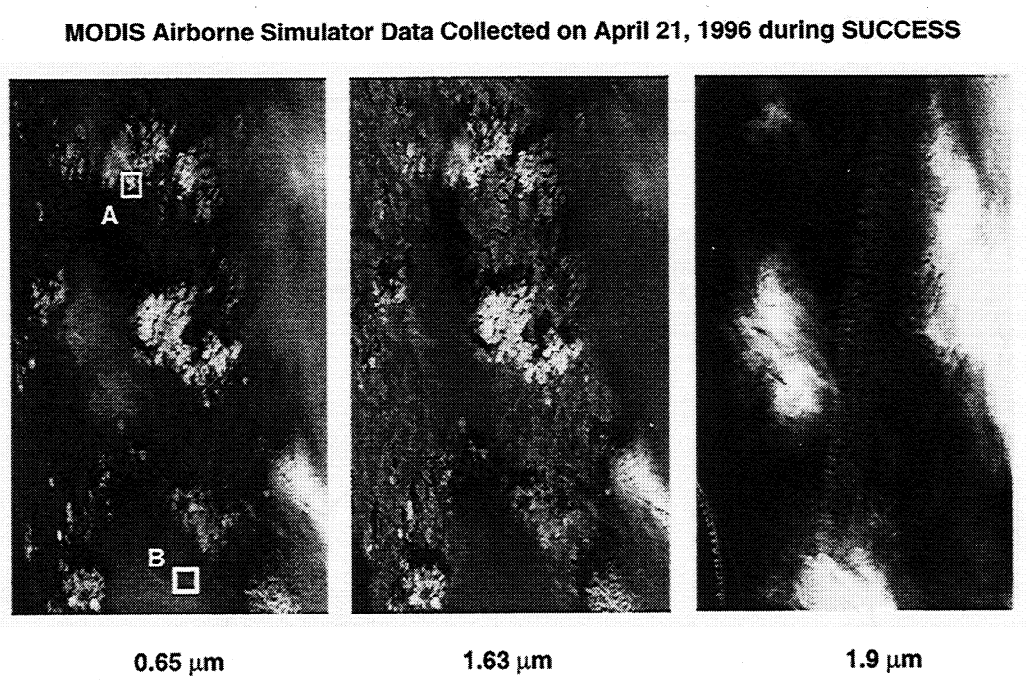

Figure 8. MAS image recorded on April 21, 1996, over Oklahoma during ER-2 Flight Leg 11 at approximately 2000 UTC. The data in the image represent an imager swath of 37.5 km in width by 50 km in length. The boxes represent where MAS data are selected for the purposes of comparison with radiative transfer simulations (box A, low-altitude water cloud; box B, ice cloud).

dimensional effects (i.e., bumpiness at the cloud top) at the 50-m resolution of the MAS. Further analysis has revealed that the MAS nonopaque cloud data belong primarily to the cloud edges.

Figure 9c shows the behavior of the difference between the brightness temperatures at 3.82 and 11 μm [BTD(3.82-11)] as a function of 11-μm brightness temperature and 0.65-μm cloud optical thickness. Figure 9d shows the behavior of the difference between the brightness temperatures at 8.52 and 11 μm [BTD(8.52-11)] as a function of 11-μm brightness temperature and 0.65-μm cloud optical thickness. From comparison of the data with theory, one might infer that the opaque cloud pixels have a visible optical thickness greater than 20 and an effective radius of 4 μm. The cloud mean effective radius inferred from the brightness temperature difference (BTD) analysis is slightly larger than that inferred from the analysis in Figures 9a and 9b. The BTD data tend to display more scatter than the NIR reflectance data. It is difficult to say with any certainty what causes the scatter in the MAS BTD(8.52-11) data. Part of the difficulty is that with water-phase clouds, theoretical calculations underscore the limited dynamic range expected for BTD(8.52-11) values. Instrument noise, variations in surface emissivity, radiances measured at cloud edge, and band-to-band registration offsets are possible contributors to the data scatter and bear further investigation.

It is interesting to note that in each of the four panels the combination of theory and data indicates the presence of a relatively high optical thickness cloud ($\tau > 20$) composed of water droplets having an effective radius in the neighborhood of 4 μm. The results demonstrate some consistency between each of the MAS band combinations used in the retrieval.

5.2. Ice-Phase Clouds

Figure 10 shows the MAS data from the cirrus in region B of Figure 8 superimposed over radiative transfer results. Again, visible optical thicknesses are provided for a reference. The four curves generated from theory follow the effective size of the distribution, ranging from 9 μm (cold Ci) to 78.5 μm (Ci uncinus). Figures 10a and 10b show the 1.63- and 2.15-μm MAS reflectances as a function of the visible band reflectance. The data indicate that the cirrus optical thicknesses range from slightly less than 3 to 5. The MAS data lie closest to the Cs curve, indicating that the cirrus have generally the same particle size of 19 μm.

The 3.82-μm radiance has both a solar reflected and a thermally emitted component. The radiance at 3.82-μm spans several orders of magnitude from cold temperatures (200 K) to warmer temperatures (300 K), so small variations in radiance imply significant variations in brightness temperature. Since the brightness temperatures are sensitive to both solar reflected radiance and Earth-emitted radiance, modeling the 3.82-μm band is difficult. Several studies have used the brightness temperature difference (BTD) between the 3.82- and the 11-μm bands [*Stone et al.*, 1990; *Baum et al.*, 1994] to infer cloud properties. As shown in Figure 10c in a comparison of MAS BTD(3.82-11) data to theoretical BTD(3.82-11) values, the cloud optical thicknesses range from 2.5 to 5. However, the MAS data lie between the Ci (T = -40°C) and Ci uncinus curves, indicating that the effective particle size for these pixels falls between 37 and 78.5 μm, which is larger than 19 μm as indicated by analysis of cloud reflectances calculated for the 1.63- and 1.9-μm bands in

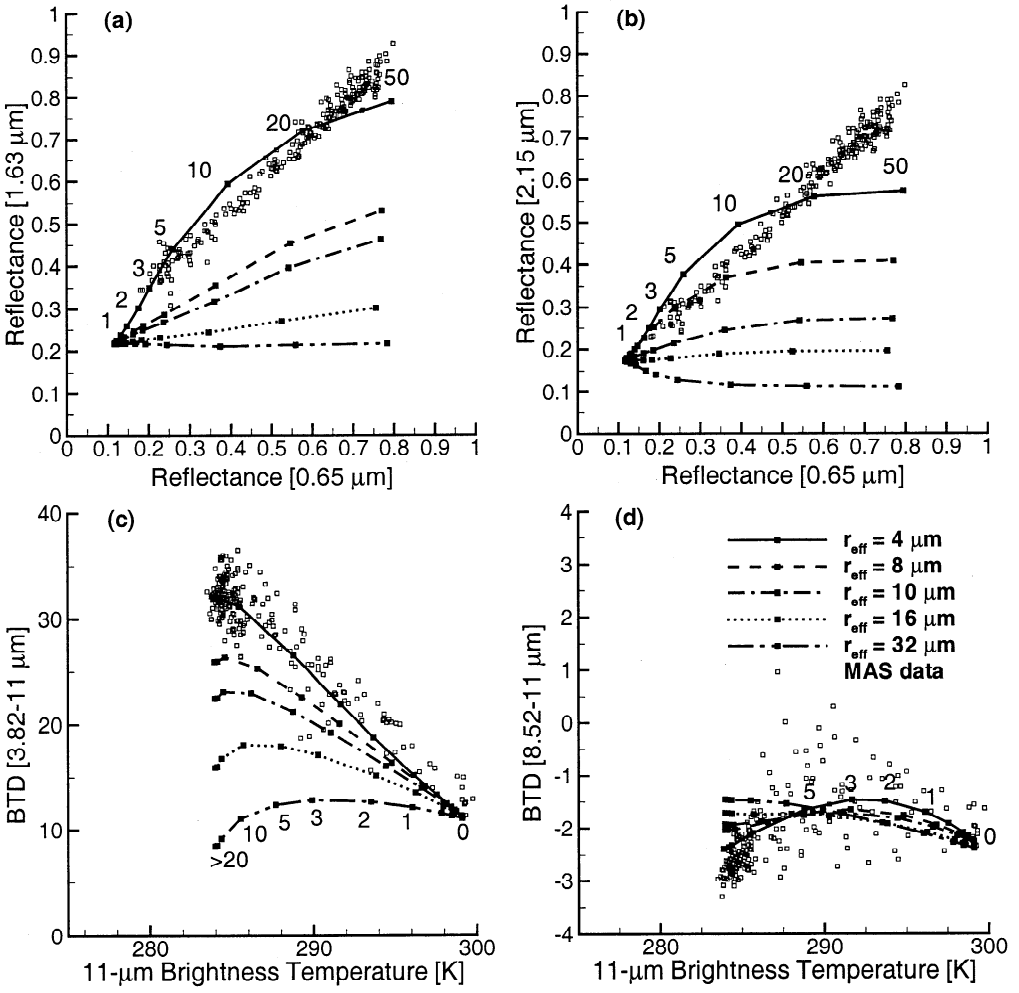

Figure 9. Comparison of theoretical results with MAS reflectance and brightness temperature difference (BTD) measurements recorded from a low-level water-phase cloud on April 21, 1996, from region A (see Figure 8). Results are shown for (a) the reflectance at 1.63 μm versus the reflectance at 0.65 μm; (b) the reflectance at 2.15 μm versus the reflectance at 0.65 μm; (c) the BTD(3.82-11 μm) versus the 11-μm brightness temperature; and (d) the BTD(8.52-11 μm) versus the 11-μm brightness temperature. Visible (0.65 μm) optical thicknesses are provided on the curves.

Figures 10a and 10b. There is more variation in the MAS BTD data compared to the reflectances, which is due in part to the sensitivity of the 3.82-μm BT to the reflected solar component.

Figure 10d shows the BTD(8.52-11) as a function of 11-μm BT and 0.65-μm cloud optical thickness. The 0.65-μm optical thicknesses range from 2.5 to 5, similar to results in Figures 10a-10c. The MAS data primarily lie between the Cs curve (effective size = 19.3 μm) and the Ci uncinus curve (effective size = 78.5 μm). While scattering of solar radiation is important for analysis of the 3.82-μm radiances, scattering is almost negligible in the 8.52-μm band. It is interesting to note the greater spread of MAS data in the 8.52-μm band than with the other bands.

The results indicate that the estimates of optical thickness are consistent among various bands. However, estimates of cloud mean particle size, inferred from comparing theoretical calculations with the data for each band, show less consistency. The lack of consistency may be due to several factors, such as the ice particle shape assumed in the derivation of the scattering properties, the size distribution, the assumed mix of shapes in the size distribution, and also errors in instrument calibration. We do not currently have detailed information of scattering properties for individual ice-crystal habits over a wider size range. When these data become available, we will perform a thorough sensitivity analysis to investigate some of the uncertainties found in the results of Figure 10.

6. Summary

We have developed an approach to infer cloud properties, such as cloud optical thickness, cloud thermodynamic phase, cloud particle size, and cloud overlap by comparing cloud and clear-sky radiative transfer computations to MAS measurements during the SUCCESS field campaign during April and May 1996. For the wavelengths used in our analyses (0.65, 1.63, 1.90, 2.15,

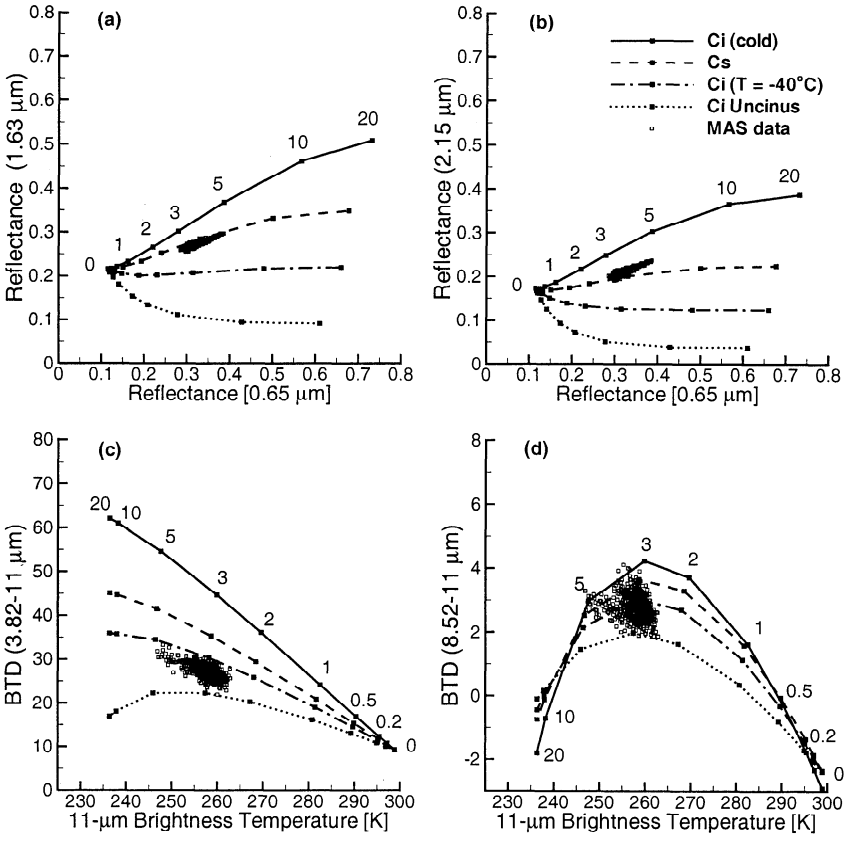

Figure 10. Comparison of theoretical results with MAS reflectance and BTD measurements recorded from a cirrus cloud on April 21, 1996, from region B (see Figure 8). Results are shown for (a) the reflectance at 1.63 μm versus the reflectance at 0.65 μm; (b) the reflectance at 2.15 μm versus the reflectance at 0.65 μm; (c) the BTD(3.82-11 μm) versus the 11-μm brightness temperature, and (d) the BTD(8.52-11 μm) versus the 11-μm brightness temperature. Visible (0.65 μm) optical thicknesses are provided in the curves.

3.82, 8.52, 11, and 12 μm), clear-sky absorption due to water vapor, ozone, and other trace gases is calculated using a set of correlated *k*-distribution routines developed specifically for this set of MAS bands. For each of the wavelengths listed above, scattering properties (phase function, single-scattering albedo, and extinction cross section) are utilized for both water droplet and ice-phase clouds. Scattering properties for ice phase clouds are incorporated for seven cirrus models. The cirrus are composed of four crystal types: hexagonal plates, two-dimensional bullet rosettes, hollow columns, and aggregates.

Results from comparison of MAS data from a liquid water cloud with theoretical results indicate that estimates of optical thickness and particle size are consistent with one another no matter which bands are used in the analysis.

The comparison of MAS data from a cirrus cloud with theoretical calculations show that the range of estimates of optical thickness are consistent among the various bands selected for comparison. Interestingly, the estimates of particle size are not consistent among the various band combinations. The main source of the uncertainty seems to be with the interpretation of the 3.82-μm MAS data, which is one of the most difficult to model due to the sensitivity of measured radiances at this wavelength to both reflected sunlight and thermal infrared emission. When we obtain a more extensive set of cirrus scattering properties we will perform a thorough sensitivity study to determine the sensitivity of the theoretical calculations to the assumed size distribution or to the assumed distribution of ice-crystal shapes.

Appendix

It is sometimes expedient to perform radiative transfer calculations with truncated phase functions; this is primarily due to the strong forward peaks of the actual phase functions at 0.65-, 1.63-, 1.90-, and 3.82-μm wavelengths. To achieve the same result in multiple-scattering computations with the truncated phase functions as with the nontruncated phase functions, an adjustment must be made to the optical thickness and single-scattering albedo. For both water- and ice-phase clouds, there is a strong contribution in the forward scattering direction due to diffraction. An additonal contribution to the strong forward peaks of the phase functions of polyhedral ice crystals is caused by δ transmission through parallel planes of the polyhedral crystals at a scattering angle of 0° [*Takano and Liou*, 1989a]. The fractions of scattered energy residing in the forward peak due to diffraction f and δ-transmission f_δ are removed from the scattering parameters using the similarity principle. Primes are used to denote the radiative parameters adjusted for diffraction. Double primes are used to denote the scattering parameters adjusted for both diffraction and δ transmission through opposing basal planes.

The extinction optical thickness (τ) is the sum of of the

scattering (τ_s) and absorption (τ_a) optical thicknesses. Since the strong diffraction forward peak has no contribution from absorption, the adjusted scattering and absorption optical thicknesses are

$$\tau'_s = (1-f)\tau_s, \tag{5}$$

$$\tau'_a = \tau_a. \tag{6}$$

The adjusted extinction optical thickness is then

$$\tau' = \tau'_s + \tau'_a = (1-f\tilde{\omega})\tau. \tag{7}$$

The adjusted single-scattering albedo may be expressed as

$$\tilde{\omega}' = \frac{\tau'_s}{\tau'} = \frac{(1-f)\tilde{\omega}}{1-f\tilde{\omega}}. \tag{8}$$

To adjust the scattering parameters for δ-transmission, a second adjustment is made similarly to that in equations (6) and (7), so the extinction optical thickness and single-scattering albedo become

$$\tau'' = (1-f_\delta\tilde{\omega})\tau, \tag{9}$$

$$\tilde{\omega}'' = \frac{(1-f_\delta)\tilde{\omega}}{1-f_\delta\tilde{\omega}}. \tag{10}$$

As *Takano and Liou* [1989a] point out, the expressions for optical thickness and single-scattering albedo scaled for both diffraction and δ transmission can be simplified to

$$\tau'' = (1-f''\tilde{\omega}')\tau', \tag{11}$$

$$\tilde{\omega}'' = \frac{(1-f'')\tilde{\omega}'}{1-f''\tilde{\omega}'}, \tag{12}$$

where

$$f'' = f + f_\delta - ff_\delta. \tag{13}$$

Again, there is no δ-transmission adjustment for water droplet clouds. Further, the δ transmission becomes very small at longer wavelengths because of increasing absorption.

Acknowledgments. Work on the derivation of ice-crystal scattering properties was supported by a MODIS contract to UCLA (contract NAG5-6160). The authors express their appreciation to the useful comments from two anonymous reviewers and from Chris Moeller and Andrew Heymsfield. The authors also thank Liam Gumley for providing the MAS imaging software.

References

Arnott, W. P., Y. Y. Dong, J. Hallett, and M. R. Poellot, Role of small ice crystals in radiative properties of cirrus: A case study, FIRE II, November 22, 1991, *J. Geophys. Res.*, *99*, 1371-1381, 1994.

Baum, B. A., and J. D. Spinhirne, Remote sensing of cloud properties using MODIS airborne simulator imagery during SUCCESS, 3, Cloud overlap, *J. Geophys. Res.*, this issue.

Baum, B. A., R. F. Arduini, B. A. Wielicki, P. Minnis, and S-C. Tsay, Multilevel cloud retrieval using multispectral HIRS and AVHRR data: Nighttime oceanic analysis, *J. Geophys. Res.*, *99*, 5499-5514, 1994.

Baum, B. A., P. F. Soulen, K. I. Strabala, M. D. King, S. A. Ackerman, W. P. Menzel, and P. Yang, Remote sensing of cloud properties using MODIS airborne simulator imagery during SUCCESS, 2, Cloud thermodynamic phase, *J. Geophys. Res.*, this issue.

Downing, H. D., and D. Williams, Optical constants of water in the infrared, *J. Geophys. Res.*, *80*, 1656-1661, 1975.

Gosse, S., D. Labrie, and P. Chylek, Refractive index of ice in the 1.4-7.8 μm spectral range, *Appl. Opt.*, *34*, 6582-6586, 1995.

Hansen, J. E., and L. D. Travis, Light scattering in planetary atmospheres, *Space Sci. Rev.*, *16*, 527-610, 1974.

Heymsfield, A. J., Cirrus uncinus generating cells and the evolution of cirroform clouds, part I, Aircraft observations of the growth of the ice phase, *J. Atmos. Sci.*, *32*, 799-808, 1975.

Heymsfield, A. J., and C. M. R. Platt, A parameterization of the particle size spectrum of ice clouds in terms of the ambient temperature and the ice water content, *J. Atmos. Sci.*, *41*, 846- 855, 1984.

Heymsfield, A. J., K. M. Miller, and J. D. Spinhirne, The 27-28 October 1986 FIRE IFO Cirrus Case Study: Cloud microstructure, *Mon. Weather Rev.*, *118*, 2313-2328, 1990.

King, M. D., et al., Airborne scanning spectrometer for remote sensing of cloud, aerosol, water vapor, and surface properties, *J. Atmos. Oceanic Technol.*, *13*, 777-794, 1996.

Kratz, D. P., The correlated *k*-distribution technique as applied to the AVHRR bands, *J. Quant. Spectrosc. Radiat. Transfer*, *53*, 501-517, 1995.

Kratz, D. P., and F. G. Rose, Accounting for molecular absorption within the spectral range of the CERES window band, *J. Quant. Spectrosc. Radiat. Transfer*, *61*, 83-95, 1999.

Kurucz, R. L., I. Furenlid, J. Brault, and L. Testerman, Solar flux atlas from 296 to 1300 nm, in *National Solar Observatory Atlas no. 1*, 239 pp., Nat. Solar Obs., Sunspot, N. M., 1984.

Lawson, R. P., A. J. Heymsfield, S. M. Aulenbach, and T. L. Jensen, Shapes, sizes, and light scattering properties of ice crystals in cirrus and a persistent contrail during SUCCESS, *Geophys. Res. Lett.*, *25*, 1331-1334, 1998.

Moeller, C. C., P. S. Grant, D. D. LaPorte, L. E. Gumley, P. Hajek, W. P. Menzel, J. S. Myers, and S. White, Blackbody emissivity considerations for radiometric calibration of the MODIS Airborne Simulator (MAS) thermal bands, *SPIE*, *2820*, 44-55, 1996.

Moeller, C. C., D. D. LaPorte, P. Hajek, K. I. Strabala, and W. P. Menzel, Spectral characterization of MODIS Airborne Simulator (MAS) LWIR bands and application to MODIS science data cloud products, *SPIE*, *3117*, 235-243, 1997.

Neckel, H., and D. Labs, The solar radiation between 3300 and 12500 angstroms, *Sol. Phys.*, *90*, 205-258, 1984.

Platt, C.M.R, and A. C. Dilley, Remote sounding of high clouds, II, Infrared emissivity of cirrostratus, *J. Appl. Meteorol.*, *18*, 1144-1150, 1979.

Press, W. H., B. P. Flannery, S. A. Teukolsky, and W. T. Vetterling, *Numerical Recipes*, 839 pp., Cambridge Univ. Press, New York, 1986.

Sassen, K., C. J. Grund, J. Spinhirne, M. Hardesty, and J. M. Alvarez, The 27-28 October 1986 FIRE IFO cirrus case study: A five lidar overview of cloud structure and evolution, *Mon. Weather Rev.*, *118*, 2288-2311, 1990.

Smith, W. L., et al., Observations of the infrared radiative properties of the ocean—Implications for the measurement of sea surface temperature via satellite remote sensing, *Bull. Am. Meteorol. Soc.*, *77*, 41-51, 1996.

Spinhirne, J. D., and W. D. Hart, Cirrus structure and radiative parameters from airborne lidar and spectral radiometer observations: The 28 October case study, *Mon. Weather Rev.*, *118*, 2329-2343, 1990.

Stone, R. S., G. L. Stephens, C. M. R. Platt, and S. Banks, The remote sensing of thin cirrus cloud using satellites, lidar and radiative transfer theory, *J. Appl. Meteorol.*, *29*, 353-366, 1990.

Takano, Y., and K.-N. Liou, Solar radiative transfer in cirrus clouds, part 1, Single-scattering and optical properties of hexagonal ice crystals, *J. Atmos. Sci.*, *46*, 3-19, 1989a.

Takano, Y., and K.-N. Liou, Solar radiative transfer in cirrus clouds, part 2, Theory and computation of multiple scattering in an anisotropic medium, *J. Atmos. Sci.*, *46*, 20-36, 1989b.

Toon, O. B., and R. C. Miake-Lye, Subsonic aircraft: Contrail and cloud effects special study (SUCCESS), *Geophys. Res. Lett.*, *25*, 1109-1112, 1998.

Tsay, S.-C., K. Stamnes, and K. Jayaweera, Radiative transfer in stratified atmospheres: Development and verification of a unified model, *J. Quant. Spectrosc. Radiat.Transfer*, *43*, 133- 148, 1990.

Warren, S. G., Optical constants of ice from the ultraviolet to the microwave, *Appl. Opt.*, *23*, 1206-1225, 1984.

Wielicki, B. A., and L. Parker, On the determination of cloud cover from satellite sensors: The effect of sensor spatial resolution, *J. Geophys. Res.*, *97*, 12,799-12,823, 1992.

Wiscombe, W. J., Improved Mie scattering algorithm, *Appl. Opt.*, *19*, 1505-1507, 1980.

Wyser, K., and P. Yang, Average ice crystal size and bulk shortwave single scattering properties for cirrus clouds, *Atmos. Res.*, *49*, 315-335, 1998.

Yang, P., and K.N. Liou, Finite-difference time domain method for light scattering by small ice crystals in three-dimensional space, *J. Opt. Soc. Am. A.*, *13*, 2072-2085,1996a.

Yang, P., and K.N. Liou, Geometric-optics-integral-equation method for light scattering by nonspherical ice crystals, *Appl. Opt.*, *35*, 6568-6584, 1996b.

Yang, P., and K. N. Liou, Single-scattering properties of complex ice crystals in terrestrial atmosphere, *Contrib. Atmos. Phys.*, *71*, 223-248, 1998.

Yang, P., K.N. Liou, and W. P. Arnott, Extinction efficiency and single-scattering albedo for laboratory and natural cirrus clouds, *J. Geophys. Res.*, *102*, 21,825-21,835, 1997.

B. A. Baum, NASA/CIMS, 1225 West Dayton St., Madison, WI 53706. (bryan.baum@ssec.wisc.edu).

Y. Hu, NASA Langley Research Center, Hampton, VA 23681-2199.

D. P. Kratz, NASA Langley Research Center, Hampton, VA 23681-2199.

S. C. Ou, Department of Atmospheric Sciences, University of California at Los Angeles, CA 90032.

P. F. Soulen, Joint Center for Earth Systems Technology, University of Maryland, Baltimore County, Catonsville, MD 21228.

S.-C. Tsay, NASA Goddard Space Flight Center, Greenbelt, MD 20771.

(Received May 21, 1999; revised October 6, 1999;
accepted October 13, 1999.)